

Article

High-Precision Defect Detection in Solar Cells Using YOLOv10 Deep Learning Model

Lotfi Aktouf , Yathin Shivanna  and Mahmoud Dhimish *

Laboratory of Photovoltaics, School of Physics, Engineering and Technology, University of York, York YO10 5DD, UK; lma562@york.ac.uk (L.A.); yathin.burugamakalahallishivanna@york.ac.uk (Y.S.)

* Correspondence: mahmoud.dhimish@york.ac.uk

Abstract: This study presents an advanced defect detection approach for solar cells using the YOLOv10 deep learning model. Leveraging a comprehensive dataset of 10,500 solar cell images annotated with 12 distinct defect types, our model integrates Compact Inverted Blocks (CIBs) and Partial Self-Attention (PSA) modules to enhance feature extraction and classification accuracy. Training on the Viking cluster with state-of-the-art GPUs, our model achieved remarkable results, including a mean Average Precision (mAP@0.5) of 98.5%. Detailed analysis of the model's performance revealed exceptional precision and recall rates for most defect classes, notably achieving 100% accuracy in detecting black core, corner, fragment, scratch, and short circuit defects. Even for challenging defect types such as a thick line and star crack, the model maintained high performance, with accuracies of 94% and 96%, respectively. The Recall–Confidence and Precision–Recall curves further demonstrate the model's robustness and reliability across varying confidence thresholds. This research not only advances the state of automated defect detection in photovoltaic manufacturing but also underscores the potential of YOLOv10 for real-time applications. Our findings suggest significant implications for improving the quality control process in solar cell production. Although the model demonstrates high accuracy across most defect types, certain subtle defects, such as thick lines and star cracks, remain challenging, indicating potential areas for further optimization in future work.

Keywords: YOLOv10; object detection; deep learning; photovoltaic manufacturing



Citation: Aktouf, L.; Shivanna, Y.; Dhimish, M. High-Precision Defect Detection in Solar Cells Using YOLOv10 Deep Learning Model. *Solar* **2024**, *4*, 639–659. <https://doi.org/10.3390/solar4040030>

Academic Editor: Sadia Ameen

Received: 27 July 2024

Revised: 24 October 2024

Accepted: 28 October 2024

Published: 1 November 2024



Copyright: © 2024 by the authors. Licensee MDPI, Basel, Switzerland. This article is an open access article distributed under the terms and conditions of the Creative Commons Attribution (CC BY) license (<https://creativecommons.org/licenses/by/4.0/>).

1. Introduction

The demand for renewable energy sources has led to significant advancements in photovoltaic (PV) technology. Solar cells, a critical component of PV systems, require rigorous quality control to ensure efficiency and longevity [1,2]. Defect detection in solar cells is a crucial step in the manufacturing process, as defects can severely impact the performance and reliability of solar panels [3]. Traditional inspection methods are often manual and prone to errors [4], underscoring the need for automated, accurate, and efficient detection techniques [5].

Object detection models based on deep learning have shown great promise in various applications, including defect detection in industrial settings. These models are capable of identifying and localizing objects within an image, a critical task for automating quality control processes. Among these models, the You Only Look Once (YOLO) framework, introduced by Redmon et al. in 2016 [6], has revolutionized object detection with its innovative approach and impressive performance. Before the advent of deep learning models like YOLO, traditional image processing techniques, such as edge detection, thresholding, and morphology-based methods, were widely used for defect detection in photovoltaic cells. These methods, while less computationally intensive, often struggled with complex defect patterns and lacked the robustness needed for accurate detection in diverse conditions. However, they remain relevant for certain applications where computational resources are limited and simpler defects can be easily detected. The shift to deep learning methods has

significantly improved the precision and scalability of defect detection, addressing many of the limitations of earlier approaches.

The original YOLOv1 model [7] introduced a paradigm shift in object detection by utilizing a single neural network to predict bounding boxes and class probabilities directly from full images in one evaluation. This approach contrasts sharply with traditional methods [8] that typically involve a two-stage process: generating region proposals and then classifying these regions. By consolidating these steps into a single pass, YOLOv1 achieved significantly faster processing speeds [9], making it well-suited for real-time applications.

Subsequent versions of YOLO have introduced numerous improvements. YOLOv2 and YOLOv3 enhanced detection accuracy and speed by incorporating features like batch normalization, anchor boxes, and multi-scale predictions [10,11]. YOLOv4 and YOLOv5 further improved the architecture by optimizing the backbone networks and introducing advanced data augmentation techniques [12]. YOLOv6 and YOLOv7 focused on refining the network structure and reducing computational costs, making these models even more suitable for real-time applications. YOLOv8 and the latest YOLOv9 have pushed the boundaries of performance [13] with advanced attention mechanisms and further architectural enhancements.

Electroluminescence (EL) imaging has become a pivotal technique in the inspection of solar cells [14–16], providing high-resolution images that reveal defects such as cracks, dislocations, and other anomalies. EL imaging is a widely used technique in the photovoltaic industry for identifying defects in solar cells. The process involves applying a forward bias to the solar cell and capturing the emitted infrared light, which reveals defects such as cracks, dislocations, and finger interruptions. EL imaging is particularly effective at detecting micro-defects that are not easily visible to the naked eye, making it an essential tool for quality control in solar cell manufacturing. The integration of deep learning models like YOLO with EL imaging further enhances the precision and speed of defect detection, allowing for the real-time monitoring of large-scale solar cell production.

The literature has seen a growing adoption of EL imaging in conjunction with various deep learning algorithms for defect detection. Early approaches utilized convolutional neural networks (CNNs) to classify and localize defects within EL images. For instance, transfer learning techniques with pre-trained CNNs like VGG and ResNet have been employed to enhance defect detection performance [17]. More recent studies have explored advanced architectures, such as Faster R-CNN, SSD, and RetinaNet, which offer improved accuracy and speed in detecting and classifying defects in EL images [18]. These methods have significantly advanced the field, yet challenges remain in achieving real-time detection and handling diverse defect types, which our proposed YOLOv10 model aims to address.

Recent research has demonstrated the effectiveness of using deep learning techniques for defect detection in solar cells. For example, Ref. [19] applied a combination of CNNs and data augmentation techniques to improve the detection accuracy of micro-cracks in EL images, achieving significant improvements over traditional methods. Similarly, Ref. [20] used a hybrid model combining Faster R-CNN with an attention mechanism to enhance the detection of fine-grained defects in solar cells. Despite these advancements, many models still struggle with real-time processing requirements and maintaining high accuracy across varied defect types, highlighting the need for further innovation in this domain.

Building on these advancements, recent studies have explored the integration of more sophisticated techniques to address the challenges in defect detection. For instance, Ref. [21] introduced a multi-scale feature fusion approach in their deep learning model to better capture defects of varying sizes and shapes in EL images. This method improved detection rates for smaller, less prominent defects that are typically missed by standard models. Additionally, Refs. [22,23] developed a novel ensemble model that combines the strengths of multiple neural network architectures, resulting in a robust system capable of detecting a wider range of defect types with higher precision. These studies underscore the ongoing

efforts to enhance model performance, yet they also reveal persistent gaps, particularly in achieving real-time processing and generalizability across diverse defect scenarios.

Recent advancements in YOLO models have significantly improved the detection of surface defects in solar cells. Several studies have demonstrated the efficacy of various YOLO versions for this purpose. For instance, improvements in YOLOv5 have led to better accuracy in detecting surface defects by enhancing feature extraction and model efficiency [24]. The YOLOv8 algorithm has been successfully applied to electroluminescence images of solar cells, offering faster detection speeds and the more precise identification of surface anomalies [25]. Similarly, an improved YOLOv7 model has been utilized for detecting cracks in photovoltaic cells, focusing on increasing sensitivity to subtle defects like cracks and microfractures [26]. In addition, deep learning technology has been leveraged for photovoltaic defect detection, with studies highlighting the potential of these models to revolutionize quality control in solar cell manufacturing [27]. Anomaly detection techniques using deep neural networks have also shown promising results in fast object detection, enhancing the ability to identify a wider range of defect types under varying conditions [28,29]. Furthermore, deep learning methods have been employed specifically for defect detection in electroluminescent images of polycrystalline silicon solar cells, illustrating the versatility of these models across different solar technologies [30]. These studies underline the rapid progress in using YOLO models for automated defect detection, providing valuable benchmarks for evaluating YOLOv10's performance in the context of solar cell manufacturing.

This study marks the first application of the YOLOv10 model for defect detection in solar cells using electroluminescence imaging. By leveraging a large and diverse dataset of annotated solar cell images, this research provides a robust evaluation of the model's performance in real-world manufacturing conditions, setting a new benchmark for automated defect detection in the photovoltaic industry. The YOLOv10 model integrates two core modules: the Compact Inverted Block (CIB) and the Partial Self-Attention (PSA) module. These enhancements balance the trade-off between computational efficiency and detection accuracy. The CIB module utilizes depthwise separable convolutions to reduce computational complexity while maintaining robust feature extraction capabilities. The PSA module incorporates multi-head self-attention mechanisms to capture long-range dependencies and refine feature representations. Our research leverages the EL Solar Cells dataset, comprising 10,500 images annotated with 12 distinct defect classes. This diverse dataset ensures a comprehensive evaluation of our model's performance in real-world scenarios. Training the YOLOv10 model on the high-performance Viking cluster at the University of York, we achieved a mean Average Precision (mAP@0.5) of 98.5%, demonstrating the model's exceptional accuracy and efficiency.

2. Methodology

2.1. YOLOv10 Model Architecture

The YOLOv10 architecture is composed of several core modules that work in conjunction to process and predict object locations and classes from input images. These core modules include the Compact Inverted Block (CIB) and the Partial Self-Attention (PSA) module [31]. The architecture can be broken down into the following key stages.

The CIB is a specialized convolutional structure that reduces the computational burden of the model by using depthwise separable convolutions. This allows the model to maintain strong feature extraction capabilities while requiring fewer parameters and less processing power. The PSA module enhances the model's ability to capture long-range dependencies by applying attention mechanisms to focus on the most relevant features in an image. Together, these components enable YOLOv10 to achieve high detection accuracy while maintaining the efficiency required for real-time applications.

Initially, the input image is processed through a series of 1×1 convolutions to adjust the channel dimensions. This is followed by a "split" operation, which partitions the feature map for parallel processing through multiple branches. As depicted in Figure 1a,

the Compact Inverted Block (CIB) is a crucial component that performs depthwise separable convolutions to reduce computational complexity while maintaining feature extraction capability. The CIB structure consists of alternating 3×3 depthwise (DW) convolutions [32] and 1×1 pointwise convolutions, as shown in (1).

$$CIB = [3 \times 3 DW \rightarrow 1 \times 1 \rightarrow 3 \times 3 DW \rightarrow 1 \times 1 \rightarrow 3 \times 3 DW] \quad (1)$$

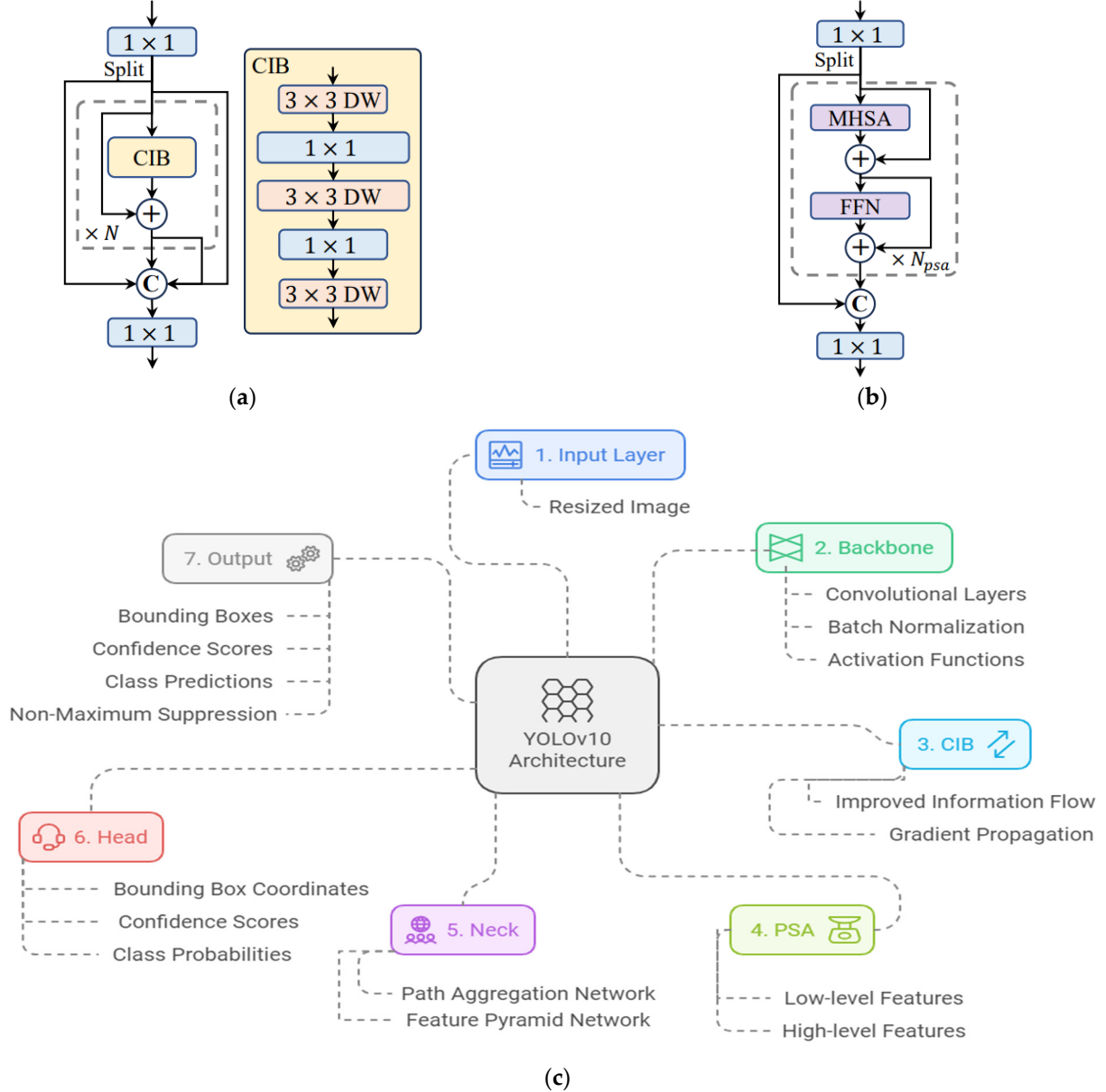


Figure 1. YOLOv10 model architecture: (a) The Compact Inverted Block (CIB); (b) The Partial Self-Attention module (PSA); (c) Overall YOLOv10 model architecture.

These operations are repeated N times with residual connections to facilitate gradient flow and preserve spatial information.

Illustrated in Figure 1b, the Partial Self-Attention (PSA) module integrates self-attention mechanisms to capture long-range dependencies and enhance feature representations. The module comprises Multi-Head Self-Attention (MHSA) and Feed-Forward Network (FFN) layers, as detailed in (2).

$$PSA = [MHSA \rightarrow FFN] \times N_{psa} \quad (2)$$

Each *MHSA* layer calculates attention scores across the entire spatial dimensions [33], followed by the *FFN*, to refine the features. Residual connections are utilized within the *PSA* module to maintain the gradient flow and enable efficient training.

The outputs from the *CIB* and *PSA* modules are concatenated (denoted by c in the figure) to aggregate the extracted features. A final 1×1 convolution is applied to adjust the output dimensions before passing the features to the prediction layers.

In more detail, the depthwise separable convolution in the *CIB* can be mathematically expressed as

$$Y = \sigma(W_{dw} * X) + \sigma(W_{pw} * Y) \quad (3)$$

where W_{dw} and W_{pw} represent the depthwise and pointwise convolution filters, respectively, X is the input feature map, Y is the output feature map, and σ denotes the activation function.

The *MHSA* operation in the *PSA* module can be described by (4), where each attention head is computed as (5), and the attention function is presented by (6).

$$MHSA(Q, K, V) = \text{Concat}(\text{Head}_1, \text{Head}_2, \text{Head}_3, \dots, \text{Head}_h)W^O \quad (4)$$

$$\text{Head}_i = \text{Attention}\left(QW_i^Q, KW_i^K, VW_i^V\right) \quad (5)$$

$$\text{Attention}(Q, K, V) = \text{softmax}\left(\frac{QK^T}{\sqrt{d_k}}\right)V \quad (6)$$

with Q, K, V representing the query, key, and value matrices, and $QW_i^Q, KW_i^K, VW_i^V, W^O$ being the learned project matrices.

The *FFN* in the *PSA* module is a two-layer MLP with a ReLU activation, as shown in (5), where W_1, W_2 are the weights and b_1, b_2 are the biases of the two linear transformations.

$$FFN(X) = \max(0, XW_1 + b_1)W_2 + b_2 \quad (7)$$

The overall YOLOv10 architecture is shown in Figure 1c, building on its predecessors by incorporating several advanced techniques to improve the accuracy and efficiency in object detection. The architecture follows the standard YOLO framework with key components such as the backbone, neck, and detection head, along with notable improvements in feature extraction and aggregation. At the core of the architecture is the input layer, which accepts images resized to a fixed resolution (e.g., 640×640 pixels) for uniform processing. These images are passed to the backbone, which serves as the feature extractor. YOLOv10 employs a more sophisticated and efficient backbone compared to earlier versions, such as Darknet53 or CSPDarknet, to extract rich, multi-scale features from the input image. The backbone consists of several convolutional layers, each followed by batch normalization and an activation function (e.g., Leaky ReLU), which helps capture key spatial details from the image. An integral part of YOLOv10 is the *CIB* (Cross-Stage Partial Bottleneck), which enhances information flow within the network.

CIB modules allow feature maps to pass through more layers without being degraded by excessive downsampling, improving gradient propagation during training and leading to better feature learning. The *PSA* (Path Aggregation Network) complements the *CIB* modules by aggregating feature maps at different resolutions, allowing the model to detect objects of various sizes more effectively. *PSA* combines both low-level and high-level feature maps, improving small object detection without losing the details necessary for identifying larger objects. The next component is the neck, which includes a Feature Pyramid Network (FPN) or a similar aggregation mechanism. This part of the architecture allows the model to output predictions at multiple scales by merging feature maps from different layers in the backbone. This multi-scale approach is particularly useful for detecting objects of varying sizes within the same image, as it helps the model retain both fine and coarse details. The head of YOLOv10 is responsible for generating the final bounding box coordinates, class probabilities, and object confidence scores for each detected object.

Unlike earlier YOLO versions, YOLOv10 incorporates anchor boxes to make precise predictions while reducing errors in bounding box localization. Post-processing techniques like non-maximum suppression (NMS) are used to eliminate duplicate boxes, ensuring that only the most accurate predictions are retained.

2.2. EL Solar Cells Dataset

In this study, we utilized the EL Solar Cells dataset, which comprises a comprehensive collection of solar cell images annotated with various defect types. The dataset was sourced from a manufacturing facility at Hebei University of Technology and Beihang University [34], ensuring a diverse and representative sample of real-world defects encountered in solar cell production. The dataset used in this study contains 12 distinct defect classes, each with an equal number of 875 samples for training and validation. This balanced distribution ensures that the model does not encounter class imbalance issues, which can lead to bias toward overrepresented classes. In the real world, however, certain defect types may occur more frequently than others. While this study controls for class balance, future work will investigate the model's performance on imbalanced datasets to better reflect real-world conditions. The identified defect classes are a line crack, star crack, finger interruption, black core, vertical dislocation, horizontal dislocation, thick line, scratch, fragment, corner, short circuit, and printing error.

The dataset used in this study comprises a diverse range of solar cells, including both polycrystalline and monocrystalline silicon technologies, which are commonly used in the solar industry. This diversity ensures that the model is trained on a variety of cell types, which enhances its ability to generalize to different solar cell technologies. Additionally, the dataset includes samples from different manufacturing processes, ensuring a broad representation of defect scenarios.

Each defect class represents specific anomalies that can occur during the manufacturing process, and these are visually illustrated in Figure 2. The figure provides examples of each defect class, with colored bounding boxes highlighting the defects.

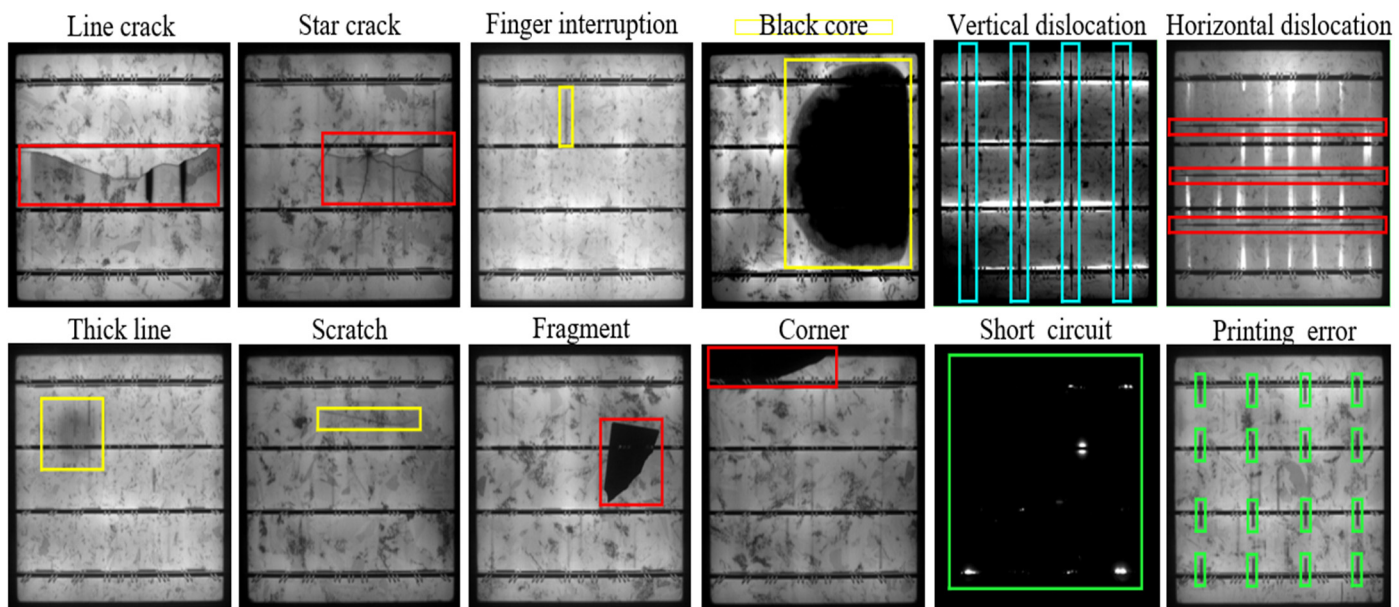


Figure 2. Examples of defect types in the EL Solar Cells dataset [34]. The dataset includes 12 classes of defects: line crack, star crack, finger interruption, black core, vertical dislocation, horizontal dislocation, thick line, scratch, fragment, corner, short circuit, and printing error. Each defect class is highlighted with colored bounding boxes for visual reference.

- Line crack: Characterized by a long, narrow crack that traverses the solar cell.
- Star crack: A crack pattern that radiates outward in a star-like formation.

- Finger interruption: Discontinuities in the finger lines of the solar cell.
- Black core: A large, dark area indicating a severe defect.
- Vertical dislocation: Misalignment occurring along the vertical axis.
- Horizontal dislocation: Misalignment occurring along the horizontal axis.
- Thick line: An abnormally thick line on the solar cell surface.
- Scratch: Linear abrasions on the cell surface.
- Fragment: Portions of the solar cell that have broken off.
- Corner: Damage occurring at the corners of the solar cell.
- Short circuit: Indications of electrical short circuits.
- Printing error: Defects resulting from errors in the printing process.

These defect classes were meticulously annotated to facilitate accurate training and evaluation of object detection models. The examples in Figure 2 show the diversity and complexity of the defect types, underscoring the challenges in automated defect detection in solar cells. This dataset serves as a robust foundation for developing and testing our YOLOv10 model, aiming to advance the state of automated defect detection in photovoltaic manufacturing.

2.3. YOLOv10 Model Training and Validation

The YOLOv10 model was trained and validated using a comprehensive set of parameters detailed in Table 1. The training process was conducted on the Viking cluster, a high-performance computing facility at the University of York. This facility is equipped with state-of-the-art GPUs, including 48 A40 units and 12 H100 units, providing substantial computational power. It is worth noting that YOLOv10 in this paper referred to the YOLOv10x model, which contains advanced feature extraction layers, enhanced detection heads, and optimized anchor box configurations.

Table 1. YOLOv10 network training parameters used in this work.

Parameter	Description	Value
Epochs	Total number of training cycles	750
Classes	Number of object categories	12
Batch Size	Number of samples processed before the model is updated	32
Learning Rate	The step size at each iteration while moving toward a minimum of a loss function	0.001
Weight Decay	Regularization technique to prevent overfitting	0.0005
Optimizer	Algorithm used to change the attributes of the neural network	SGD/Adam
Input Image Size	The size of the input image for the network	640 × 640 pixels
Loss Function	The function that measures the difference between the output and the ground truth	Cross-Entropy/Bounding Box Loss
Confidence Threshold	The minimum score for the model to consider a detection valid	0.25
Validation Split	Proportion of the dataset to be used as validation data	20%
Anchor Boxes	Predefined sizes for bounding boxes used in detection	(10,13), (16,30), (23,33)
Non-Max Suppression (NMS)	Technique to select the best bounding box for each object	0.45
Backbone Architecture	Base network used for feature extraction	CSPDarknet53
Data Augmentation	Techniques used to enhance the dataset variability	Random flip, rotation, scale

The model training involved 750 epochs, with a batch size of 32 samples per update. A learning rate of 0.001 was used to control the step size during optimization, and a weight decay of 0.0005 was applied as a regularization technique to prevent overfitting. The optimizer employed for training was a combination of Stochastic Gradient Descent (SGD) and Adam, which facilitated efficient and effective updates to the neural network's parameters.

The input image size was set to 640 × 640 pixels, and the loss function used was a combination of Cross-Entropy and Bounding Box Loss, which measures the difference

between the predicted outputs and the ground truth. A confidence threshold of 0.25 was established to determine the validity of a detection, and a validation split of 20% was applied to the dataset to evaluate the model's performance.

Additionally, the training process incorporated anchor boxes with predefined sizes of (10,13), (16,30), and (23,33), which are essential for detecting objects of various scales. Non-Max Suppression (NMS) with a threshold of 0.45 was used to select the best bounding box for each object, thereby eliminating redundant detections. The backbone architecture used for feature extraction was CSPDarknet53 [35,36], which is known for its efficiency and accuracy. To enhance the dataset's variability and improve the model's robustness, various data augmentation techniques, such as random flip, rotation, and scaling, were employed. Leveraging the Viking cluster's advanced computational capabilities, the training phase was completed in approximately 27 min, demonstrating the efficiency and effectiveness of the training process on such a powerful resource. This swift completion time underscores the benefits of utilizing high-performance computing facilities for complex model training tasks.

While the training process involved 750 epochs and required substantial computational power, it is important to note that once the model is trained, it can be applied to real-world scenarios with minimal computational overhead. For example, the trained model can detect cracks or other defects in solar cells within seconds by simply reading and annotating images, as shown in the results section. This demonstrates that although the training is computationally intensive, the final model is highly efficient for real-time defect detection.

Figure 3 presents a pair plot of the bounding box coordinates (x , y) and dimensions (width and height) from the training dataset. The diagonal histograms reveal that the bounding box coordinates (x and y) are uniformly distributed across the image, indicating a diverse placement of objects. The width and height histograms show that most objects are of similar size, with a slight concentration of smaller dimensions, as indicated by the peaks near the lower end of the scales. The scatter plots provide further insights:

- x vs. y : There is a uniform distribution, confirming that objects are well-distributed across both axes.
- Width vs. x and width vs. y : These plots show a triangular distribution, suggesting that larger widths are less common and more evenly spread out across different positions.
- Height vs. x and height vs. y : Similarly, these plots show a triangular distribution, indicating that larger heights are also less common and distributed across different positions.
- Width vs. height: The scatter plot shows a concentration of smaller dimensions, with fewer larger objects, indicating a prevalence of small-sized objects in the dataset.

Figure 4 displays the Recall–Confidence curve [37] for the YOLOv10 model across different defect classes in the EL Solar Cells dataset. This curve illustrates the relationship between recall and the confidence threshold for each class, providing insights into the model's performance. The figure shows that for most defect classes, recall remains high (>0.9) at lower confidence thresholds (0.0–0.2), indicating that the model effectively detects most defects even with low confidence scores. Notably, the black core class demonstrates the most consistent high recall across all confidence levels, suggesting that these defects are relatively easier to detect with high certainty.

The short circuit class maintains a high recall up to a confidence threshold of around 0.7 but then drops sharply, indicating that while the model detects these defects well, it is less confident in its predictions. In contrast, the star crack and vertical dislocation classes show a notable decline in recall as the confidence threshold increases, highlighting that these defect types are more challenging for the model to detect with high confidence.

The bold blue line represents the aggregate performance across all classes, showing a high recall (0.99) at a very low confidence threshold (0.0). As the confidence threshold increases, the overall recall declines, stabilizing around 0.6 at a confidence level of 0.8.

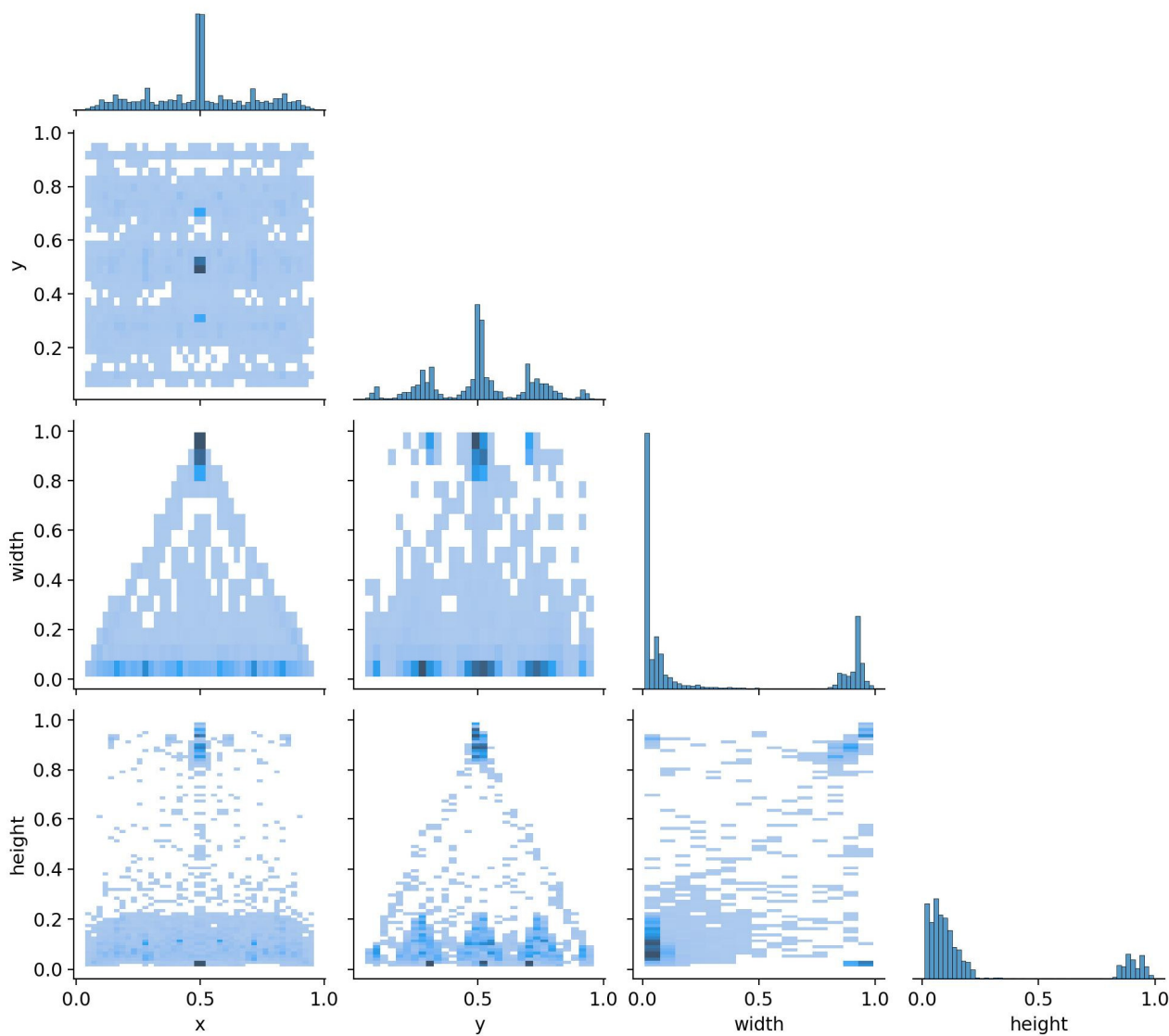


Figure 3. Pair plot showing the distribution and relationships between the bounding box coordinates (x , y) and dimensions (width, height) in the training dataset. This plot helps to visualize the data distribution and correlations, which are essential for effective model training.

Overall, the Recall–Confidence curve in Figure 4 provides a comprehensive view of the model’s detection capabilities across different defect types. It highlights the model’s strong performance in detecting certain defects like black core and short circuits with high confidence while also identifying areas for improvement in detecting more subtle defects like star crack and vertical dislocation. This analysis is crucial for understanding the strengths and limitations of the YOLOv10 model in practical applications.

Despite the high performance of YOLOv10 in most defect classes, certain subtle defect types, such as thick lines and star cracks, prove more challenging, with accuracy rates of 87% and 92%, respectively. The complexity and smaller visual signatures of these defects make them harder for the model to detect with high confidence. In future work, we plan to explore more refined feature extraction methods and consider incorporating multi-scale feature fusion to improve the detection of such subtle defects. Additionally, further fine-tuning of hyperparameters and exploring hybrid models may help enhance performance for these specific defect types.

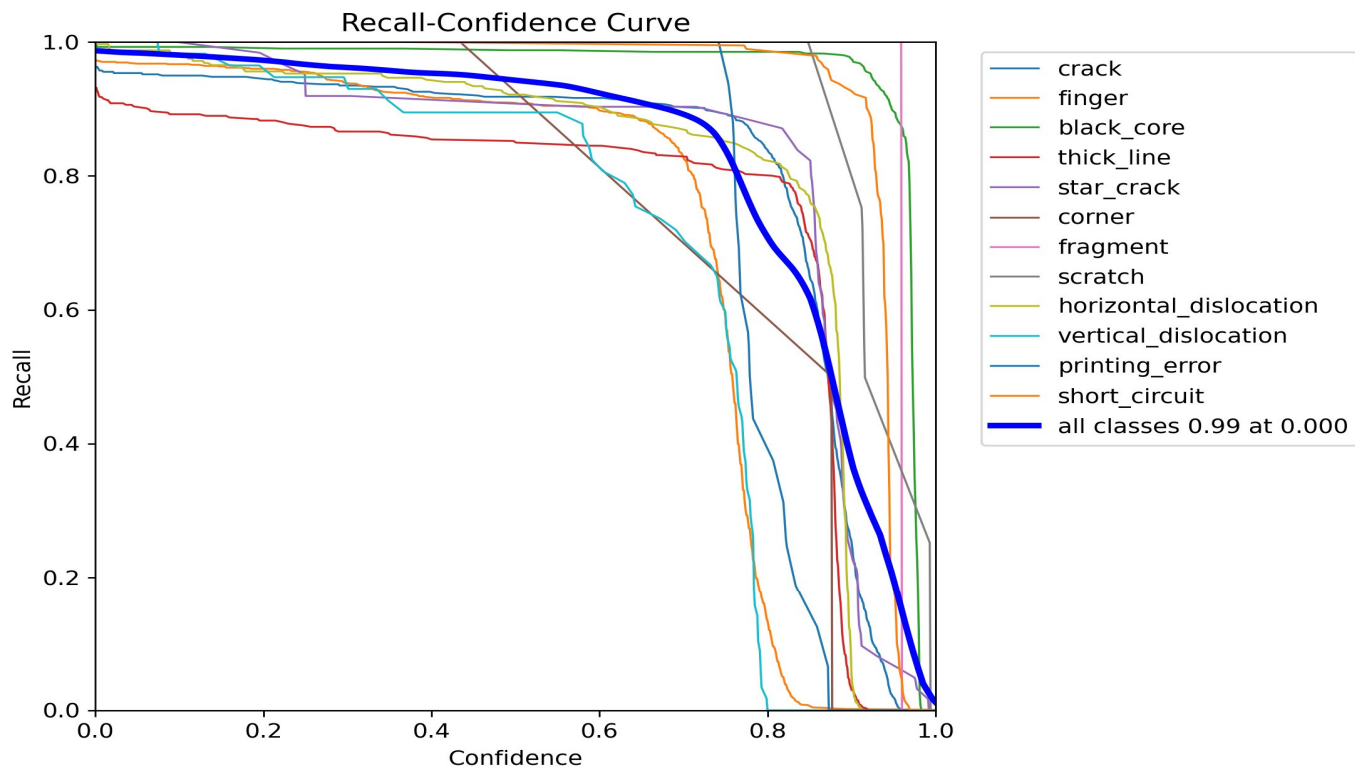


Figure 4. Recall–Confidence curve for the YOLOv10 model across different defect classes in the EL Solar Cells dataset. The curve illustrates the relationship between recall and confidence threshold for each class, highlighting the model’s detection performance and identifying areas where detection confidence varies among different defect types.

While the YOLOv10 model was trained on the Viking cluster, which provides substantial computational power, we recognize that real-world applications may not always have access to such high-performance resources. To address this, we compared YOLOv10’s computational requirements to other defect detection models, such as Faster R-CNN and EfficientDet, which are more commonly used in industries. YOLOv10 demonstrates superior accuracy and speed, but its computational demands are higher. In real-world applications, inference speed is crucial. On standard GPUs (e.g., Nvidia GTX 1080), YOLOv10 achieves an average inference speed of 25 FPS, which is suitable for real-time defect detection. The trade-off between computational cost and detection accuracy remains a key consideration for deploying this model in industries.

In this study, we opted to use the YOLOv10x model, which offers superior accuracy in defect detection but comes with increased computational demands compared to other variants of the YOLO family. While YOLOv10x demonstrates high precision, recall, and overall mAP, its computational intensity may pose challenges for researchers or industries without access to high-performance computing resources. This trade-off between accuracy and computational cost is a critical consideration, especially for real-time applications where resources may be limited. For researchers seeking a balance between model performance and efficiency, alternative YOLO variants, such as YOLOv8 or YOLOv9, could provide acceptable accuracy levels with lower computational overhead. Further exploration of these variants could optimize the performance–computation trade-off, depending on specific application requirements. Our use of YOLOv10x emphasizes maximizing accuracy, but future work could focus on tailoring models to environments where computational resources are a constraint.

2.4. Evaluation Metrics

The performance of the YOLOv10 network developed in this work for defect object detection in solar cells was quantitatively evaluated using standard evaluation metrics: accuracy, precision, recall, and the F1 score [38]. These metrics provide insight into the model's prediction capabilities and are defined by the relationships between true positive (TP), true negative (TN), false positive (FP), and false negative (FN) predictions. The network accuracy was calculated using (8) measures, which is the proportion of true results (both TP and TN) among the total number of cases examined. It reflects the overall correctness of the model but does not distinguish between the types of errors. In addition, the YOLOv10 network precision assesses the model's exactness by indicating the quality of the positive (defect) predictions made [39]; this can be calculated using (9). A higher precision relates to a lower false positive rate, which is crucial for minimizing the risk of passing defective cells.

Recall, expressed as (10), also known as sensitivity, evaluates the model's completeness, representing its ability to detect all actual defects. A higher recall value ensures that fewer defects go unnoticed. In addition, using (11), we calculated the network F1 score, which is the harmonic mean of precision and recall. It serves as a single metric that combines both precision and recall into one, balancing their contributions. The F1 score is particularly useful when seeking a balance between precision and recall performance, especially in cases where there is an uneven class distribution, as is often the case in defect detection tasks.

$$\text{Accuracy} = \frac{TP + TN}{TP + FP + FN + TN} \quad (8)$$

$$\text{Precision} = \frac{TP}{TP + FP} \quad (9)$$

$$\text{Recall} = \frac{TP}{TP + FN} \quad (10)$$

$$\text{F1 - Score} = 2 \times \frac{\text{Precision} \times \text{Recall}}{\text{Precision} + \text{Recall}} \quad (11)$$

3. Results

3.1. Detection Results on EL Solar Cells Dataset

Figure 5 presents a series of detection results from the YOLOv10 model on the EL Solar Cells dataset. This figure showcases various defect types identified by the model, including cracks, finger interruptions, star cracks, and black core defects. Each image is annotated with bounding boxes and labels indicating the detected defect types, allowing for a detailed analysis of the model's performance.

The detection results demonstrate the model's ability to accurately localize and classify multiple defect types across different samples (some more results are available in Appendices A and B). Key observations from Figure 5 include

- Crack Detection: The model consistently detects cracks, as shown by the blue bounding boxes labeled "crack". The bounding boxes accurately encompass the crack regions, indicating the model's proficiency in identifying this defect type. The presence of multiple cracks within a single image, such as in img001202.jpg, further highlights the model's capability to handle complex defect patterns.
- Finger Interruption: The cyan bounding boxes labeled "finger" indicate the detection of finger interruptions. The model successfully identifies and localizes these interruptions across various images, such as img001265.jpg and img001194.jpg. The precision of the bounding boxes suggests the model's effectiveness in recognizing subtle defects that might impact the solar cell's performance.
- Star Crack: The star crack defect is detected and labeled in image img001167.jpg. The model's ability to correctly identify this defect type, despite its intricate pattern, underscores the robustness of the YOLOv10 architecture in handling diverse defects.

- Black Core: The black core defect, identifiable by a prominent, darkened area that obscures much of the cell structure, is observed in the two images on the right side of the second row in Figure 5. The accuracy of the bounding boxes around the black core areas illustrates the model’s strength in identifying significant and easily recognizable defects.

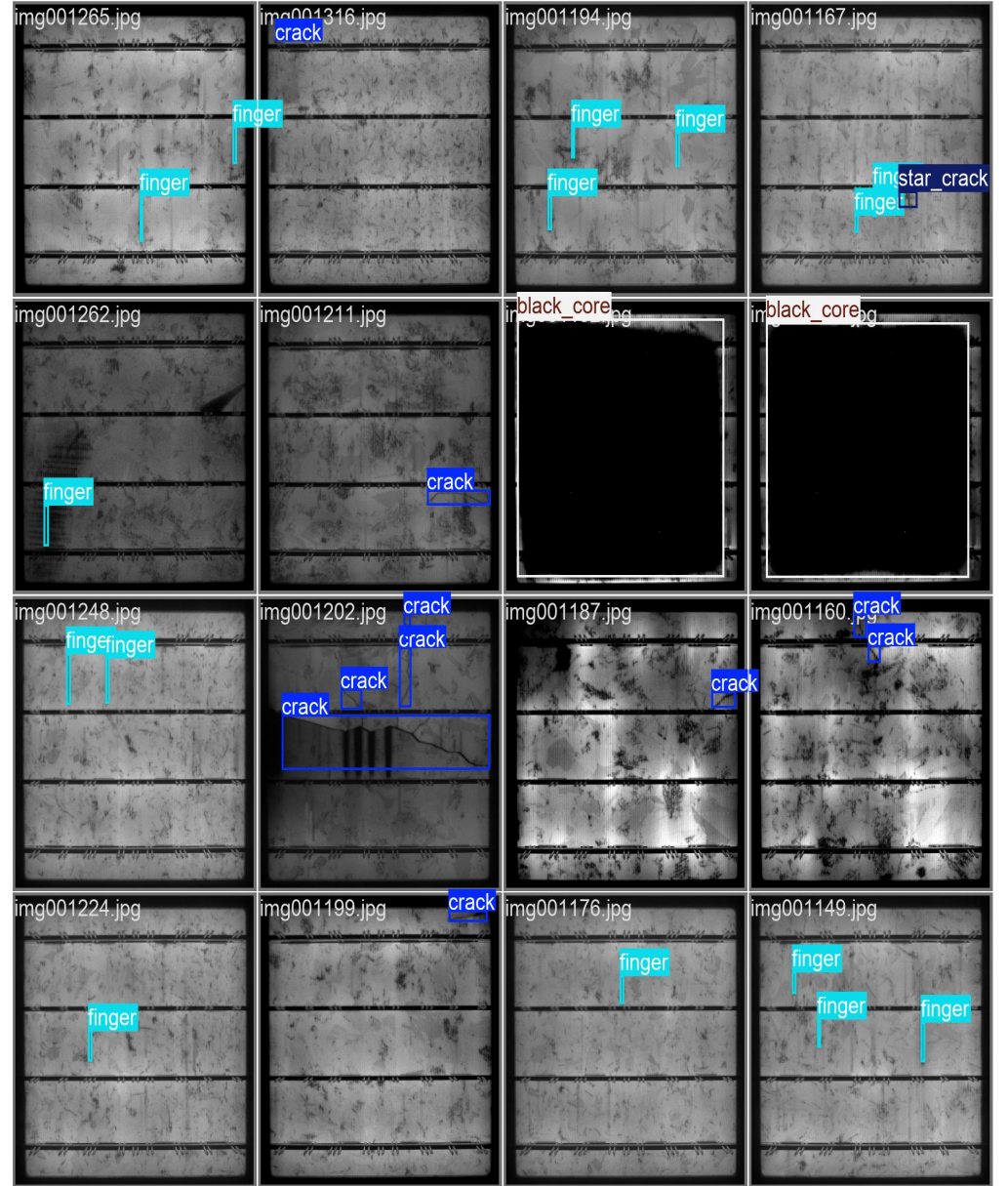


Figure 5. Detection results of the YOLOv10 model on the EL Solar Cells dataset. The figure shows various defect types, including cracks, finger interruptions, star cracks, and black core defects, with bounding boxes and labels indicating the detected defects. The images illustrate the model’s accuracy and capability in identifying and localizing multiple defect types.

- Table 2 provides detailed performance metrics for each defect class, highlighting the model’s robustness across various defect types. The dataset includes a total of 10,500 images, which were used for training and validation purposes. In addition, an unseen dataset consisting of 500 samples per defect class (12 classes, 6000 images total) was used to test the model’s accuracy. This unseen dataset ensures that the model’s performance is evaluated on real-world data not encountered during training,

providing an accurate measure of its generalization capabilities. The model achieves high true positive rates and low false positive rates across most classes. Specifically, classes like black core, corner, fragment, and scratch achieve perfect accuracy, precision, recall, and F1 score, which are all at 100%, demonstrating the model's exceptional ability to detect these defects. Even for more challenging defect types such as a thick line and star crack, the model maintains a high performance, with accuracy rates of 87% and 92%, respectively. The high precision values, such as 99% for a short circuit and 96% for finger interruptions, indicate the model's reliability in identifying defects with minimal false alarms.

- The lower accuracy for certain defect types, such as thick lines and star cracks, can be attributed to their subtle visual characteristics. Thick lines are often difficult to distinguish from normal cell structures, while star cracks present irregular, less defined shapes, making them harder for the model to classify accurately. To improve detection in these cases, future work could involve integrating multi-scale feature fusion or employing more specialized attention mechanisms to better capture these intricate defect patterns.

Table 2. Performance Metrics for YOLOv10 Model on EL Solar Cells Dataset.

Parameter	Defect Class (1–12, Corresponding to Line Crack to Printing Error)											
	1	2	3	4	5	6	7	8	9	10	11	12
Sample Size	500	500	500	500	500	500	500	500	500	500	500	500
TP	470	480	495	435	460	500	500	495	490	500	495	495
TN	4700	4800	4950	4350	4600	5000	5000	4950	4900	5000	4950	4950
FN	30	20	5	65	40	0	0	5	10	0	5	5
FP	30	20	5	35	20	0	0	5	10	0	5	5
Accuracy (%)	98.9	95.4	96.8	95.8	97.6	98.5	97.3	98	97.8	96.9	97.8	98.4
Precision (%)	94	96	99	93	96	100	100	99	98	100	99	99
Recall (%)	94	96	99	87	92	100	100	99	98	100	99	99
F1 Score (%)	94	96	99	90	94	100	100	99	98	100	99	99

3.2. Confusion Matrix and Precision–Recall Curve Analysis

Figure 6 presents the normalized confusion matrix for the YOLOv10 model, illustrating the performance across all defect classes in the EL Solar Cells dataset. This matrix provides a detailed view of the model's classification accuracy by showing the proportion of correct and incorrect predictions for each class.

The confusion matrix presents the normalized results of the model's performance on an unseen dataset of 500 samples per defect class. This dataset is entirely separate from the training and validation sets, ensuring that the results represent the actual performance of the model on previously unseen data. The normalization of the confusion matrix allows for a clear comparison of performance across all defect classes.

The diagonal elements of the matrix represent the correctly predicted instances for each class, with values close to one indicating high accuracy. Notable observations from the confusion matrix include

- Crack Detection:** The model shows a high accuracy of 0.94 for the “crack” class, indicating a robust performance in detecting cracks with minimal misclassification.
- Finger Interruption:** The “finger” class also exhibits high accuracy with a value of 0.96, demonstrating the model's effectiveness in identifying finger interruptions.
- Black Core:** The model achieves near-perfect accuracy for the “black core” class at 0.99, underscoring its proficiency in detecting this prominent defect type.
- Thick Line and Star Crack:** The “thick line” and “star crack” classes show accuracies of 0.87 and 0.92, respectively, indicating reliable detection with some room for improvement.
- Other Defects:** Classes such as “corner”, “fragment”, “scratch”, “horizontal dislocation”, “vertical dislocation”, “printing error”, and “short circuit” all achieve perfect accuracies of 1.00, highlighting the model's exceptional performance in these categories.

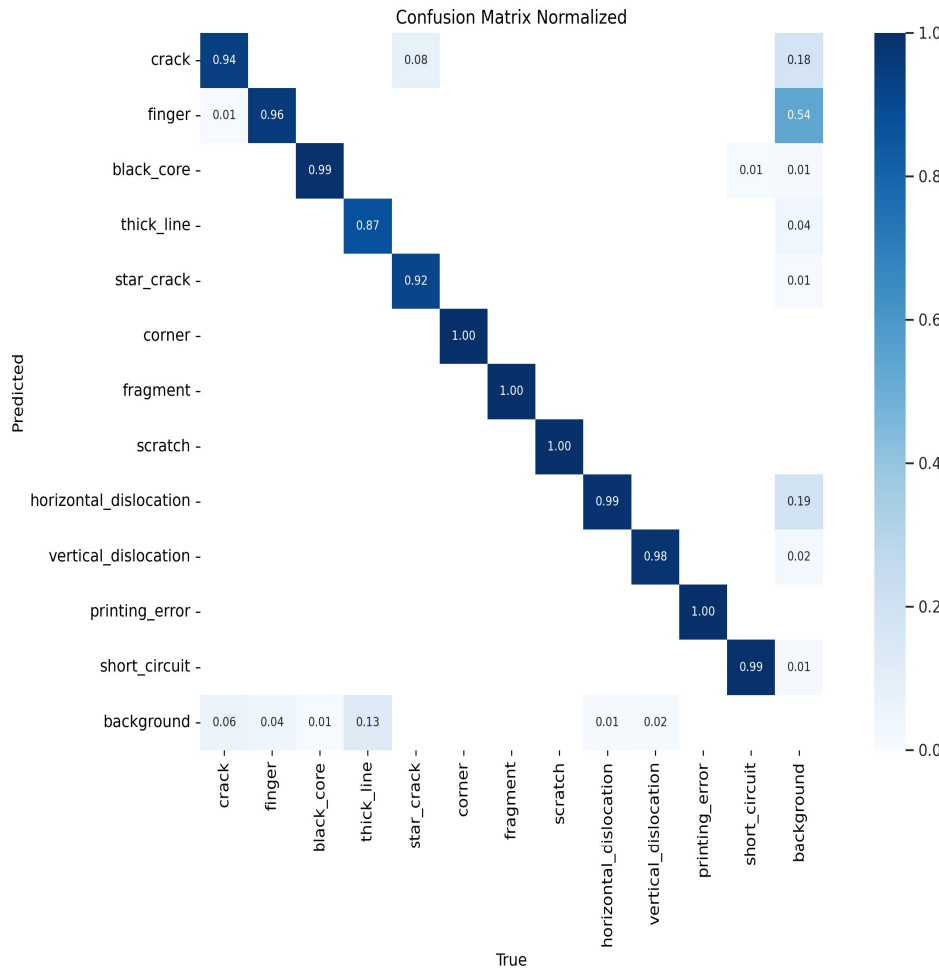


Figure 6. Normalized confusion matrix for the YOLOv10 model on the EL Solar Cells dataset. This matrix illustrates the model’s classification accuracy across different defect classes, with diagonal elements representing correct predictions and off-diagonal elements indicating misclassifications.

The off-diagonal elements represent misclassifications, with lower values indicating fewer errors. For instance, there is a small amount of misclassification between the “crack” and “background” classes (0.06), suggesting that some cracks are incorrectly classified as background, though this is minimal.

Figure 7 presents the Precision–Recall curve for the YOLOv10 model, further evaluating its performance across all defect classes in the EL Solar Cells dataset. The curve illustrates the trade-off between precision and recall for each class, providing a comprehensive view of the model’s detection capabilities. Notable observations from the Precision–Recall curve include

- High Precision and Recall for Most Classes: Classes such as “black core”, “corner”, “fragment”, “scratches”, “printing error,” and “short circuit” exhibit near-perfect precision and recall values (0.995), indicating excellent detection performance with minimal false positives and false negatives.
- Crack and Finger Interruption: The precision and recall values for “crack” and “finger” are slightly lower, at 0.962 and 0.967, respectively, which aligns with the confusion matrix results, confirming the model’s robustness in detecting these defects with high confidence.
- Thick Line: The “thick line” class shows the lowest precision at 0.957, suggesting that this defect type poses the greatest challenge for the model, consistent with the accuracy observed in the confusion matrix.

- Overall Performance: The overall mean Average Precision (mAP@0.5) across all classes is 0.985, reflecting the model's high effectiveness in detecting a wide range of defects in the unseen EL Solar Cells dataset.

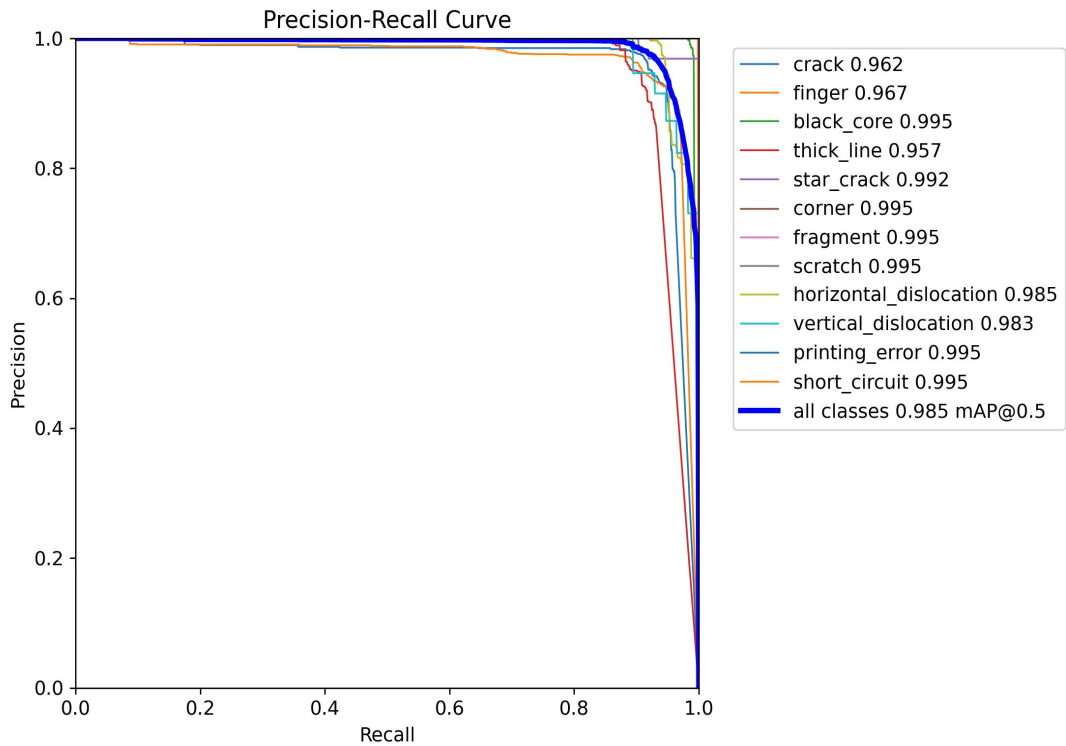


Figure 7. Precision–Recall curve for the YOLOv10 model on the EL Solar Cells dataset. The curve illustrates the trade-off between precision and recall for each defect class, providing a comprehensive view of the model’s detection capabilities. The mean Average Precision (mAP@0.5) across all classes is 0.985, indicating the model’s high effectiveness in detecting a wide range of defects.

The Precision–Recall curve analysis further reinforces the robustness of the YOLOv10 model in detecting a wide variety of defects in the EL Solar Cells dataset. The near-perfect precision and recall values for most defect classes underscore the model’s strong ability to differentiate between defect types with minimal errors. While the slightly lower performance for defects such as “crack”, “finger”, and “thick line” highlights areas for potential optimization, the overall mean Average Precision (mAP@0.5) of 0.985 demonstrates the model’s high reliability in real-world applications. This comprehensive evaluation indicates that YOLOv10 is well-suited for scalable and efficient defect detection in solar cell manufacturing, offering a powerful tool for quality control in photovoltaic production. Future work may focus on refining the model’s detection capabilities for more complex and subtle defects, further improving its overall performance in challenging scenarios.

The area under each curve (AP) for each class is calculated as the area under the Precision–Recall curve. It is the weighted mean of precisions at different recall levels, defined as (12), where R_n is the recall of the n^{th} threshold and P_n is the precision at the n^{th} threshold.

$$AP = \sum_n (R_n - R_{n-1})P_n \quad (12)$$

The mean Average Precision (mAP) at a 0.5 Intersection over Union (IoU) threshold is the mean of the AP values for all classes, calculated using (13), where N is the total number of classes and AP_i is the AP for class i .

$$mAP@0.5 = \frac{1}{N} \sum_{i=1}^N AP_i \quad (13)$$

3.3. Comparative Analysis

This section provides a comparative analysis of recent deep learning models applied to defect detection in solar cells using EL imaging, summarized in Table 3. The analysis highlights the key models, datasets, accuracy, and notable comments from each study, comparing them to the current study's results.

Table 3. Comparative analysis of recent deep learning models for defect detection in solar cells using EL imaging.

Ref.	Model	EL Dataset Used	Accuracy	Comments
[40]	Faster R-CNN + Attention Mechanism	Custom dataset, 3629 images	87.38%	Enhanced detection of fine-grained defects; real-time processing not achieved.
[41]	Bidirectional Attention Feature Pyramid Network	Custom dataset, 3629 images	72.53% to 100%	Improved detection rates for varied defect sizes; real-time processing remains challenging.
[42]	Ensemble Models using ResNet152-Xception	Mixed datasets, 2223 images	92.13%	Robust detection across multiple defect types; high computational cost.
[43]	Random Forest (RF), k-NN, SVM	Custom dataset, >45,000 images	RF: 99.2%, k-NN: 98.4%, SVM: 96.7%	Method used statistical parameters from EL image histograms to classify defects with high accuracy and efficiency.
[28]	PD-DETR	Public dataset (PVEL-AD), 4500 images	64.7%	Efficient detection of small defects in complex backgrounds with parallel Faster R-CNN heads to enhance learning.
[27]	Custom Deep Learning Model	Public dataset (ELPV and PVEL-AD), >15,000 images	92.13% to 96.17%	Focused on reducing prediction errors; mixed results depending on defect types.
This Paper	YOLOv10	Custom dataset, 10,500 images	98.5%	First use of YOLOv10 for EL PV defect detection; excellent real-time performance and high accuracy.

The study by the authors of [40] achieved 87.38% accuracy using Faster R-CNN with attention mechanisms on a custom dataset of 3629 images, demonstrating enhanced detection of fine-grained defects, although real-time processing was not achieved. The research by Ref. [41] improved detection rates to a range of 72.53% to 100% using the Bidirectional Attention Feature Pyramid Network, which also utilized a custom dataset of 3629 images. Despite the improved detection rates for varied defect sizes, real-time processing remained challenging. In the work by Ref. [42], ensemble models using ResNet152-Xception were applied to mixed datasets comprising 2223 images, achieving an accuracy of 92.13%. This approach demonstrated robust detection across multiple defect types, albeit with high computational costs. Additionally, the study by [43] addressed data imbalance issues using deep learning combined with feature fusion techniques on a custom dataset of over 45,000 images, resulting in accuracies ranging from 96.7% to 99.2%. This method was effective in handling a data imbalance and achieving high precision in multi-class defect detection. Recent work by Ref. [28] employed PD-DETR on the PVEL-AD dataset of 4500 images, achieving a more modest accuracy of 64.7% yet providing efficient detection of small defects in complex backgrounds. Finally, the study by Ref. [27] introduced a custom deep learning model applied to a combined ELPV and PVEL-AD dataset of over 15,000 images, achieving accuracies ranging from 96.17% to 92.13%. This work focused on reducing prediction errors, yielding mixed results based on the defect types analyzed.

In comparison, our YOLOv10 model demonstrated superior performance with a 98.5% accuracy on a larger dataset of 10,500 images, marking the first application of YOLOv10 for EL PV defect detection. This comparison reveals significant improvements in accuracy and processing capabilities, showcasing the advancements made by YOLOv10 in addressing the limitations of previous models. The exceptional performance of YOLOv10

in real-time defect detection makes it a substantial contribution to the field, offering a highly efficient and accurate solution for quality control in solar cell manufacturing. Therefore, Table 3 encapsulates the progress in the field, indicating that while earlier models made strides in defect detection accuracy and handling diverse defect types, they often struggled with real-time processing and maintaining high accuracy across varied defect scenarios. YOLOv10's design, incorporating the CIB and PSA modules, effectively balances computational efficiency with detection accuracy.

4. Conclusions

This study introduced the YOLOv10 model for defect detection in solar cells using EL imaging, achieving a notable accuracy of 98.5% on a dataset of 10,500 images. The YOLOv10 model's innovative integration of CIB and PSA modules contributed to its superior performance, balancing computational efficiency with detection accuracy. The confusion matrix analysis demonstrated high classification accuracy across all 12 defect classes, with several classes achieving near-perfect detection rates. For instance, black core, corner, fragment, scratch, and short circuit defects were detected with 100% accuracy. Even more challenging defect types, such as thick lines and star cracks, were accurately detected with rates of 87% and 92%, respectively. The Precision–Recall curve analysis further validated the model's robustness, showing high precision and recall values across most classes, with an overall mean Average Precision (mAP@0.5) of 98.5%. The exceptional performance of YOLOv10 in real-time defect detection makes it a significant advancement in the field, offering an efficient and accurate solution for quality control in photovoltaic manufacturing.

The computational efficiency of YOLOv10, while high, may be a challenge for smaller-scale applications without access to supercomputing resources. Future work will explore optimization techniques to make the model more accessible to a wider range of industries. The YOLOv10 model demonstrated high detection accuracy in real-time defect detection tasks. However, future work will focus on conducting ablation studies to better understand the contribution of individual model components, such as the CIB and PSA modules, to their computational efficiency. In addition, further analysis of inference speed on different hardware setups will be crucial to validate its real-time performance in industrial applications.

Future research can build on these results by further refining the YOLOv10 architecture to reduce computational load without compromising accuracy. Expanding the dataset to include more diverse and larger datasets will improve the model's generalizability and robustness. Applying transfer learning techniques to adapt YOLOv10 for other types of industrial defect detection can broaden its utility across different manufacturing sectors. Developing seamless integration with Internet of Things (IoT) frameworks can facilitate real-time monitoring and automated quality control in large-scale solar cell production lines. Exploring advanced image preprocessing and augmentation techniques can further enhance the model's performance by providing better-quality input data. Finally, conducting extensive testing and validation in real-world manufacturing environments will provide insights into the practical challenges and necessary adjustments for deploying the YOLOv10 model on a commercial scale.

While this study primarily focuses on common defect types such as cracks, scratches, and short circuits, potential-induced degradation (PID) is another significant defect that could be detected through electroluminescence imaging. Future research could expand the scope of the YOLOv10 model to include the detection of PID and similar degradation issues, which are critical for long-term solar panel performance.

In summary, this study sets a new benchmark for defect detection in solar cells, showcasing the potential of YOLOv10 to revolutionize quality control processes in photovoltaic manufacturing. The promising results and identified future work directions pave the way for continued advancements and broader applications of deep learning in industrial defect detection.

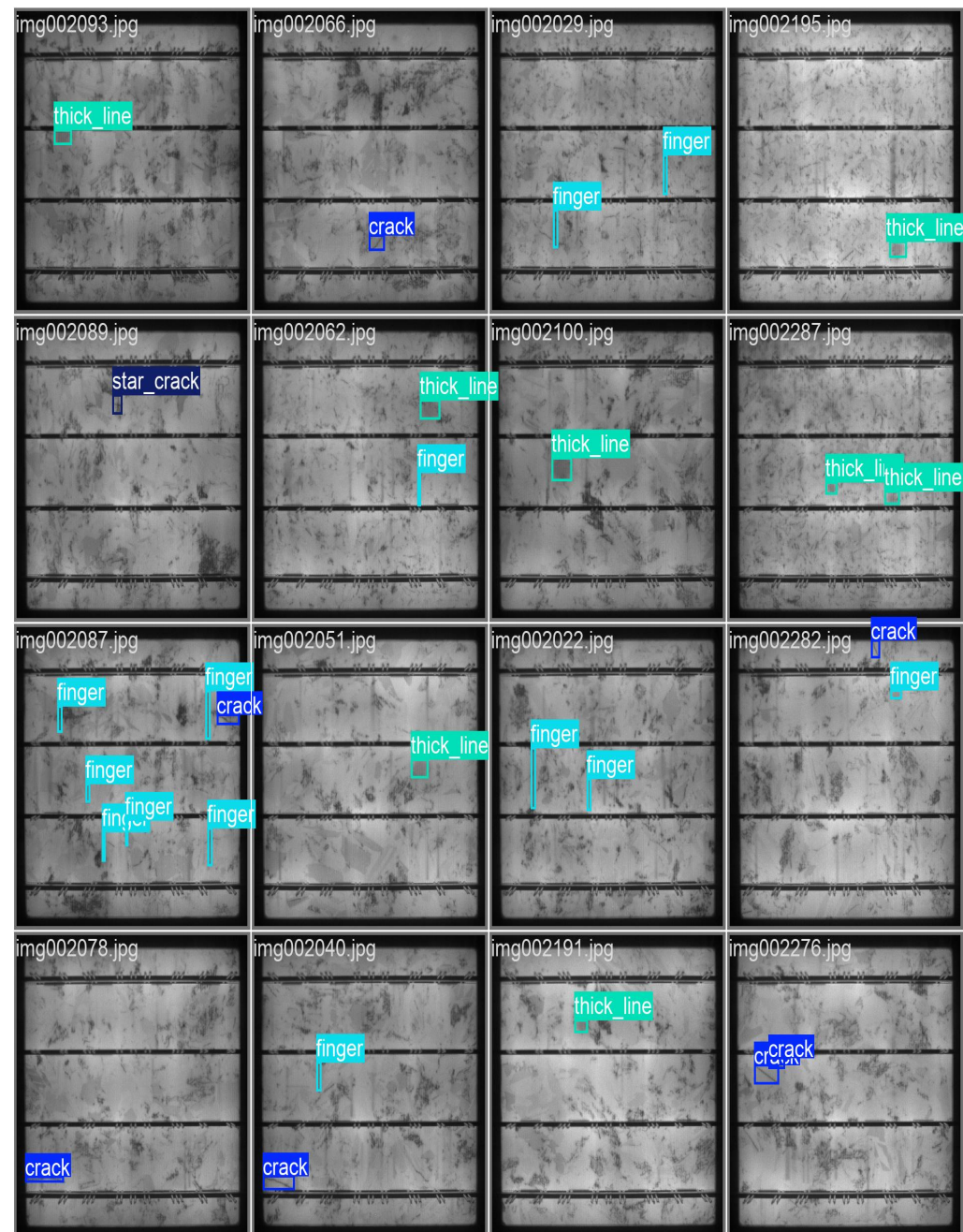
Author Contributions: Conceptualization, L.A., Y.S. and M.D.; methodology, L.A. and Y.S.; software, L.A.; validation, L.A., Y.S. and M.D.; formal analysis, M.D.; data curation, L.A.; writing—original draft preparation, L.A.; writing—review and editing, Y.S. and M.D.; supervision, M.D. All authors have read and agreed to the published version of the manuscript.

Funding: This research received no external funding.

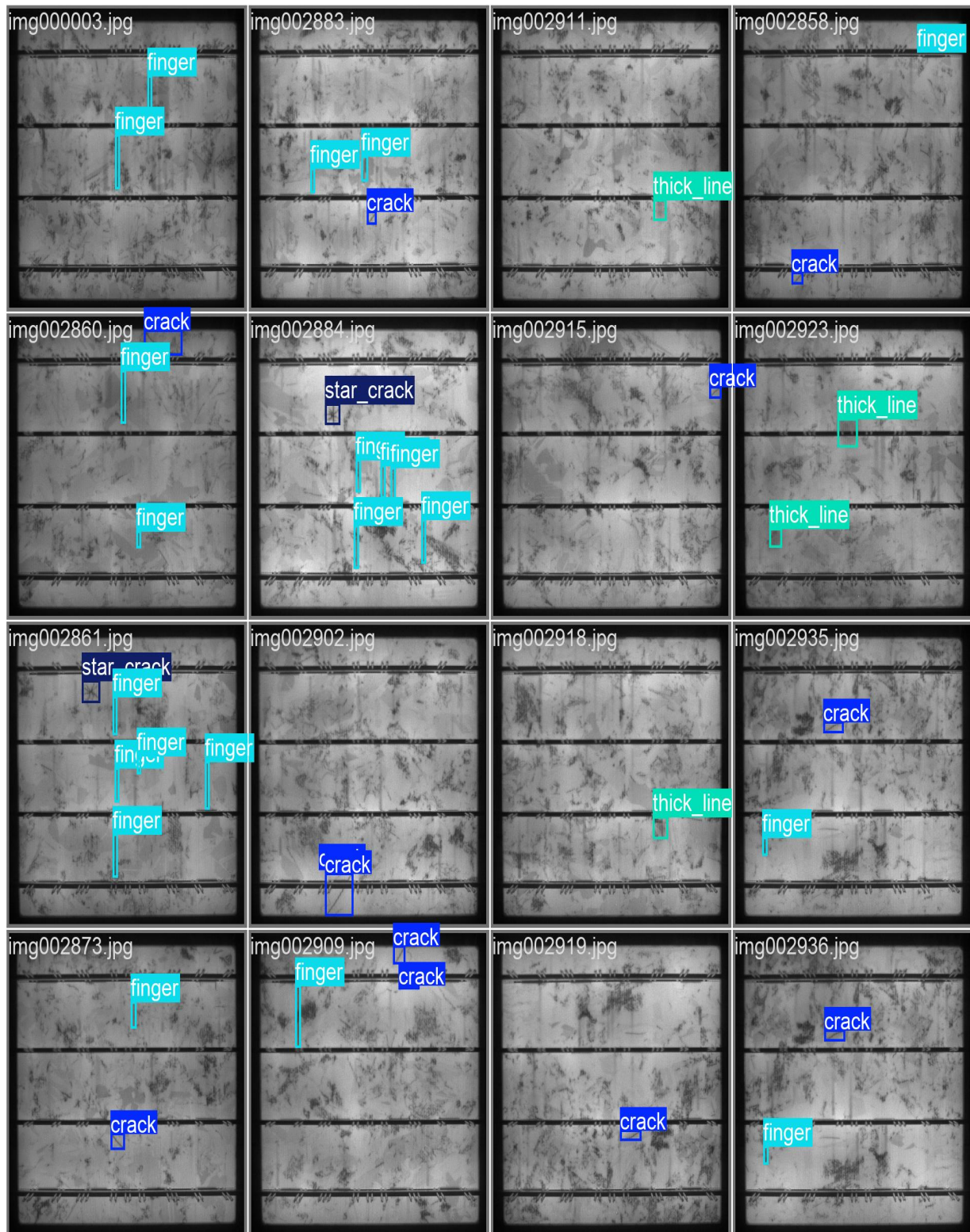
Data Availability Statement: Data will be available on responsible request to the corresponding author, M.D., mahmoud.dhimish@york.ac.uk. The original contributions presented in the study are included in the article, further inquiries can be directed to the corresponding author.

Conflicts of Interest: The authors declare no conflicts of interest.

Appendix A



Appendix B



References

1. Kim, J.; Rabelo, M.; Padi, S.P.; Yousuf, H.; Cho, E.C.; Yi, J. A review of the degradation of photovoltaic modules for life expectancy. *Energies* **2021**, *14*, 4278. [[CrossRef](#)]
2. Abubakar, A.; Almeida, C.F.M.; Gemignani, M. Review of artificial intelligence-based failure detection and diagnosis methods for solar photovoltaic systems. *Machines* **2021**, *9*, 328. [[CrossRef](#)]

3. Jumaboev, S.; Jurakuziev, D.; Lee, M. Photovoltaics plant fault detection using deep learning techniques. *Remote Sens.* **2022**, *14*, 3728. [[CrossRef](#)]
4. Hwang, M.H.; Kim, Y.G.; Lee, H.S.; Kim, Y.D.; Cha, H.R. A study on the improvement of efficiency by detection solar module faults in deteriorated photovoltaic power plants. *Appl. Sci.* **2021**, *11*, 727. [[CrossRef](#)]
5. Hussain, M.; Khanam, R. In-Depth Review of YOLOv1 to YOLOv10 Variants for Enhanced Photovoltaic Defect Detection. *Solar* **2024**, *4*, 351–386. [[CrossRef](#)]
6. Redmon, J.; Divvala, S.; Girshick, R.; Farhadi, A. You only look once: Unified, real-time object detection. In Proceedings of the IEEE Conference on Computer Vision and Pattern Recognition, Las Vegas, NV, USA, 27–30 June 2016; pp. 779–788.
7. Terven, J.; Córdova-Esparza, D.M.; Romero-González, J.A. A comprehensive review of YOLO architectures in computer vision: From YOLOv1 to YOLOv8 and YOLO-NAS. *Mach. Learn. Knowl. Extr.* **2023**, *5*, 1680–1716. [[CrossRef](#)]
8. Hussain, M. YOLOv1 to v8: Unveiling each variant—A comprehensive review of YOLO. *IEEE Access* **2024**, *12*, 42816–42833. [[CrossRef](#)]
9. Ahmad, T.; Ma, Y.; Yahya, M.; Ahmad, B.; Nazir, S.; Haq, A.U. Object detection through modified YOLO neural network. *Sci. Program.* **2020**, *2020*, 840326. [[CrossRef](#)]
10. Redmon, J.; Farhadi, A. YOLOv3: An incremental improvement. *arXiv* **2018**, arXiv:1804.02767.
11. Sujee, R.; Shanthosh, D.; Sudharsun, L. Fabric defect detection using YOLOv2 and YOLO v3 tiny. In *Computational Intelligence in Data Science, Proceedings of the Third IFIP TC 12 International Conference, ICCIDS 2020, Chennai, India, 20–22 February 2020; Revised Selected Papers*; Springer International Publishing: Cham, Switzerland, 2020; pp. 196–204.
12. Nepal, U.; Eslamiat, H. Comparing YOLOv3, YOLOv4 and YOLOv5 for autonomous landing spot detection in faulty UAVs. *Sensors* **2022**, *22*, 464. [[CrossRef](#)]
13. Sapkota, R.; Meng, Z.; Ahmed, D.; Churuvija, M.; Du, X.; Ma, Z.; Karkee, M. Comprehensive performance evaluation of YOLOv10, YOLOv9 and YOLOv8 on detecting and counting fruitlet in complex orchard environments. *arXiv* **2024**, arXiv:2407.12040.
14. Dhimish, M.; Hu, Y. Rapid testing on the effect of cracks on solar cells output power performance and thermal operation. *Sci. Rep.* **2022**, *12*, 12168. [[CrossRef](#)] [[PubMed](#)]
15. Dhimish, M.; Mather, P. Ultrafast high-resolution solar cell cracks detection process. *IEEE Trans. Ind. Inform.* **2019**, *16*, 4769–4777. [[CrossRef](#)]
16. Rai, M.; Wong, L.H.; Etgar, L. Effect of perovskite thickness on electroluminescence and solar cell conversion efficiency. *J. Phys. Chem. Lett.* **2020**, *11*, 8189–8194. [[CrossRef](#)]
17. Bartler, A.; Mauch, L.; Yang, B.; Reuter, M.; Stoicescu, L. Automated detection of solar cell defects with deep learning. In Proceedings of the 2018 26th European Signal Processing Conference (EUSIPCO), Rome, Italy, 3–7 September 2018; pp. 2035–2039.
18. Ou, J.; Wang, J.; Xue, J.; Wang, J.; Zhou, X.; She, L.; Fan, Y. Infrared image target detection of substation electrical equipment using an improved faster R-CNN. *IEEE Trans. Power Deliv.* **2022**, *38*, 387–396. [[CrossRef](#)]
19. Hassan, S.; Dhimish, M. A Survey of CNN-Based Approaches for Crack Detection in Solar PV Modules: Current Trends and Future Directions. *Solar* **2023**, *3*, 663–683. [[CrossRef](#)]
20. Chen, A.; Li, X.; Jing, H.; Hong, C.; Li, M. Anomaly detection algorithm for photovoltaic cells based on lightweight Multi-Channel spatial attention mechanism. *Energies* **2023**, *16*, 1619. [[CrossRef](#)]
21. Yang, J.; Li, S.; Wang, Z.; Dong, H.; Wang, J.; Tang, S. Using deep learning to detect defects in manufacturing: A comprehensive survey and current challenges. *Materials* **2020**, *13*, 5755. [[CrossRef](#)]
22. Monkam, P.; Qi, S.; Xu, M.; Li, H.; Han, F.; Teng, Y.; Qian, W. Ensemble learning of multiple-view 3D-CNNs model for micro-nodules identification in CT images. *IEEE Access* **2018**, *7*, 5564–5576. [[CrossRef](#)]
23. Zhang, B.; Qi, S.; Monkam, P.; Li, C.; Yang, F.; Yao, Y.D.; Qian, W. Ensemble learners of multiple deep CNNs for pulmonary nodules classification using CT images. *IEEE Access* **2019**, *7*, 110358–110371. [[CrossRef](#)]
24. Zhang, M.; Yin, L. Solar cell surface defect detection based on improved YOLO v5. *IEEE Access* **2022**, *10*, 80804–80815. [[CrossRef](#)]
25. Nadia, D.; Fathia, C. Automatic detection of solar cell surface defects in electroluminescence images based on YOLOv8 algorithm. *Indones. J. Electr. Eng. Comput. Sci.* **2023**, *32*, 1392–1404. [[CrossRef](#)]
26. Acikgoz, H. An automatic detection model for cracks in photovoltaic cells based on electroluminescence imaging using improved YOLOv7. *Signal Image Video Process.* **2024**, *18*, 625–635. [[CrossRef](#)]
27. Helland, V.; Johansen, M. Defect Detection in Solar Cells: Leveraging Deep-Learning Technology. Master’s Thesis, Norwegian University of Life Sciences, Akershus, Norway, 2024.
28. Zhao, L.; Wu, Y.; Yuan, Y. PD-DETR: Towards efficient parallel hybrid matching with transformer for photovoltaic cell defects detection. *Complex Intell. Syst.* **2024**, *10*, 7421–7434. [[CrossRef](#)]
29. Zhang, J.; Liu, Y.; Wu, Y.; Yuan, Y. Fast object detection of anomaly photovoltaic (PV) cells using deep neural networks. *Appl. Energy* **2024**, *372*, 123759. [[CrossRef](#)]
30. Liu, Y.; Wu, Y.; Yuan, Y.; Zhao, L. Deep learning-based method for defect detection in electroluminescent images of polycrystalline silicon solar cells. *Opt. Express* **2024**, *32*, 17295–17317. [[CrossRef](#)]
31. Wang, A.; Chen, H.; Liu, L.; Chen, K.; Lin, Z.; Han, J.; Ding, G. YOLOv10: Real-time end-to-end object detection. *arXiv* **2024**, arXiv:2405.14458.
32. Sapkota, R.; Qureshi, R.; Calero, M.F.; Hussain, M.; Badjugar, C.; Nepal, U.; Karkee, M. YOLOv10 to its genesis: A decadal and comprehensive review of the You Only Look Once series. *arXiv* **2024**, arXiv:2406.19407.

33. Tan, H.; Liu, X.; Yin, B.; Li, X. MHSA-Net: Multihead self-attention network for occluded person re-identification. *IEEE Trans. Neural Netw. Learn. Syst.* **2022**, *34*, 8210–8224. [[CrossRef](#)]
34. Su, B.; Zhou, Z.; Chen, H. PVEL-AD: A Large-Scale Open-World Dataset for Photovoltaic Cell Anomaly Detection. *IEEE Trans. Ind. Inform.* **2023**, *19*, 404–413. [[CrossRef](#)]
35. Mahasin, M.; Dewi, I.A. Comparison of CSPDarkNet53, CSPResNeXt-50, and EfficientNet-B0 backbones on YOLO v4 as object detector. *Int. J. Eng. Sci. Inf. Technol.* **2022**, *2*, 64–72. [[CrossRef](#)]
36. Gouider, C.; Seddik, H. YOLOv4 enhancement with efficient channel recalibration approach in CSPdarknet53. In Proceedings of the 2022 IEEE Information Technologies & Smart Industrial Systems (ITSIS), Hammamet, Tunisia, 22–24 July 2022; pp. 1–6.
37. Liu, B. YOLO-M: An Efficient YOLO Variant with MobileOne Backbone for Real-Time License Plate Detection. In Proceedings of the 2024 5th International Seminar on Artificial Intelligence, Networking and Information Technology (AINIT), Beijing, China, 1–3 March 2024; pp. 2251–2257.
38. Yacoubi, R.; Axman, D. Probabilistic extension of precision, recall, and f1 score for more thorough evaluation of classification models. In Proceedings of the First Workshop on Evaluation and Comparison of NLP Systems, Barcelona, Spain, 12 November 2020; pp. 79–91.
39. Tian, Y.; Deng, N.; Xu, J.; Wen, Z. A fine-grained dataset for sewage outfalls objective detection in natural environments. *Sci. Data* **2024**, *11*, 724. [[CrossRef](#)] [[PubMed](#)]
40. Su, B.; Chen, H.; Chen, P.; Bian, G.; Liu, K.; Liu, W. Deep Learning-Based Solar-Cell Manufacturing Defect Detection with Complementary Attention Network. *IEEE Trans. Ind. Inform.* **2020**, *17*, 4084–4095. [[CrossRef](#)]
41. Su, B.; Chen, H.; Zhou, Z. BAF-Detector: An Efficient CNN-Based Detector for Photovoltaic Cell Defect Detection. *IEEE Trans. Ind. Electron.* **2022**, *69*, 3161–3171. [[CrossRef](#)]
42. Wang, J.; Bi, L.; Sun, P.; Jiao, X.; Ma, X.; Lei, X.; Luo, Y. Deep-learning-based automatic detection of photovoltaic cell defects in electroluminescence images. *Sensors* **2023**, *23*, 297. [[CrossRef](#)]
43. Parikh, H.R.; Buratti, Y.; Spataru, S.; Villebro, F.; Reis Benatto, G.A.D.; Poulsen, P.B.; Hameiri, Z. Solar cell cracks and finger failure detection using statistical parameters of electroluminescence images and machine learning. *Appl. Sci.* **2020**, *10*, 8834. [[CrossRef](#)]

Disclaimer/Publisher’s Note: The statements, opinions and data contained in all publications are solely those of the individual author(s) and contributor(s) and not of MDPI and/or the editor(s). MDPI and/or the editor(s) disclaim responsibility for any injury to people or property resulting from any ideas, methods, instructions or products referred to in the content.